

# LIO-GVM: an Accurate, Tightly-Coupled Lidar-Inertial Odometry with Gaussian Voxel Map

Xingyu Ji<sup>1</sup>, ShengHai Yuan<sup>1</sup>, Pengyu Yin<sup>1</sup>, Lihua Xie<sup>1</sup>

**Abstract**—This letter presents an accurate and robust Lidar Inertial Odometry framework. We fuse LiDAR scans with IMU data using a tightly-coupled iterative error state Kalman filter for robust and fast localization. To achieve robust correspondence matching, we represent the LiDAR points as a set of Gaussian distributions and evaluate the divergence in variance for outlier rejection. Based on the fitted distributions, a new residual metric is proposed for the filter-based Lidar inertial odometry by incorporating both the distance and variance disparities, further enriching the comprehensiveness and accuracy of the residual metric. With the strategic design of the residual metric, we propose a simple yet effective voxel-solely mapping scheme, which only requires the maintenance of one centroid and one covariance matrix for each voxel. Experiments on different datasets demonstrate the robustness and high accuracy of our framework for various data inputs and environments. To the benefit of the robotics society, we open-source the code at [https://github.com/Ji1Xingyu/lio\\_gvm](https://github.com/Ji1Xingyu/lio_gvm).

**Index Terms**—Lidar inertial odometry, SLAM, probabilistic feature association, voxel map

## I. INTRODUCTION

THE vital requirement for an autonomous robot is to estimate its ego-motion and build a map of the environment without prior knowledge, which is widely known as Simultaneous Localization and Mapping (SLAM). In particular, the light detection and ranging (LiDAR) sensor is commonly employed because of its ability to provide light-invariant and accurate range measurements. However, the LiDAR-only SLAM system may fail in degenerate scenarios (few constraints for optimization) or high-speed applications (motion distortion in the point cloud). To address this problem, researchers combine IMU with LiDAR [1]–[6] to form a Lidar Inertial Odometry (LIO), as IMU can provide accurate short-term motion information and is insensitive to surroundings, thus can provide an initial pose guess and compensate for the distortion of LiDAR [7]. Because of the temporal and computational efficiency, filter-based LIO [4]–[6], [8], [9] has been investigated in the recent few years. The performance of a filter-based LIO system is predominantly influenced by two components: point cloud registration and mapping scheme [10]. In this letter, we aim to enhance the performance of a filter-based LIO system by addressing improvements to the shortcomings of the existing works in these two areas.

\*This work is supported by any National Research Foundation, Singapore under its Medium Sized Center for Advanced Robotics Technology Innovation.

<sup>1</sup> Authors are with the Centre for Advanced Robotics Technology Innovation (CARTIN), School of Electrical and Electronic Engineering, Nanyang Technological University, Singapore. {xingyu001, shyuan, pengyu001, elhxie}@ntu.edu.sg

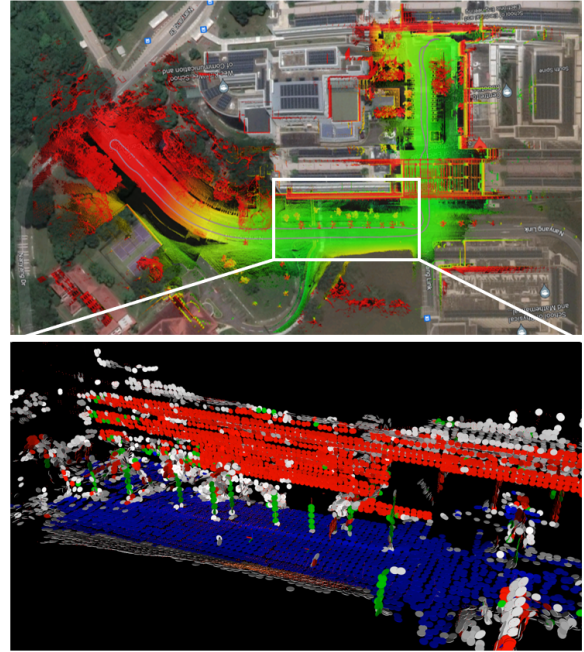


Fig. 1. The top image illustrates the global map built by LIO-GVM aligned with the Google map of Nanyang Technological University. The bottom image shows the runtime voxel map of LIO-GVM inside the rectangle. For better visualization, we model the distributions within each voxel as surfels. The blue, red, green, and white surfels denote the ground, wall, pole, and other types of voxels respectively.

For point cloud registration, LOAM [11] first proposes to extract point and line features from the source and target clouds for fast registration and achieves accurate results. MULLS [12] extends the feature types and solves the optimization via a multi-metric linear least squares method. Instead of extracting the geometric features from both the source and target domains, some systems only extract features in the target cloud and directly register the raw source cloud into the target map [8], [9]. SuMa [13] and SLICT [2] render points in the target map into surfels and perform ICP for state estimation. NDT [14] regards points in the target cloud as Gaussian distributions. GICP [15] fits the points in both the source and target clouds to Gaussian distributions. NDT tends to be more computationally efficient, while GICP is more accurate. VGICP [16] voxelizes the distributions in the target map and utilizes the voxel-based association approach, which greatly increases the efficiency while retaining comparable accuracy with GICP. LiTAMIN2 [17] introduces symmetric KL-Divergence for the residual metric, achieving accurate pose estimation even with a small number of registered points.

A common assumption of these systems is that a point in the current scan can be approximately projected to a correct feature in the target map. This projection is dominated by the combination of historical state estimations and state prediction using IMU for a LIO system. However, the accumulation of localization drifts in long-term odometry is inevitable; Simultaneously, the presence of spike noise (a severe issue in IMU, especially for low-cost ones) leads to inaccuracies in the IMU pose guess. Consequently, the validity of the assumption may be undermined by the cumulative drifts and IMU noise. Some methods choose to embed a sensor with high confidence [18] for error correction, such as GNSS. However, the drawback is that the GNSS signal is not always available in real cases. On the other hand, some other methods choose to compensate for the IMU pose estimation using Machine Learning (ML) techniques [19], [20]. Nevertheless, using ML techniques requires the ground pose and sufficient data for the training phase, which is not feasible for many practical cases.

For mapping schemes, a common method is to maintain the target map with a k-d tree [11], [21] as it can provide strict K nearest neighbor (k-NN) search for the correspondence matching. The conventional k-d tree needs to rebuild the entire tree for the map update, which is inefficient and time-consuming. FAST-LIO2 uses the ikd-Tree [22], a dynamic k-d tree that can incrementally update the map. Some systems opt to govern the target map with hash-based voxels [4], [5], [23]. Due to the requirement of the front end, these voxel-based mapping schemes need to embed a supplemental data structure (k-d tree, Hilbert Curve, etc.) within voxels to form a hierarchical structure, which leverages the rapid operation capabilities of voxels while also facilitating points management.

To cope with the problem of mismatch in point cloud registration, we represent the points in both the source and target clouds as a set of Gaussian probability distributions [14]–[16] and evaluate the matched correspondences by the disparity in variance. Moreover, based on the distribution assumption, we propose a new residual metric for filter-based LIO. The formula accesses both the distance and variance disparities, further enriching the comprehensiveness and accuracy of the residual metric. For the mapping side, instead of storing all the raw points, we propose an incremental voxel map without any additional structures, which only maintains a centroid and covariance matrix for each voxel. The idea of this simple map scheme is inspired by the following aspects: 1) With the strategic design of the residual metric, the map module only necessitates the maintenance of the centroid and covariance matrix for each distribution instead of the raw points. Similar to VGICP [16], we aggregate all the distributions within a voxel to estimate the distribution for the voxel robustly. Thus, we only need to maintain one centroid and one covariance matrix for each voxel. 2) The time complexity for the deletion, insertion, and query operations of voxels (implemented by a hash table) is  $\mathcal{O}(1)$ , which is considerably faster than the k-d tree.

In conclusion, we implement the proposed residual metric and mapping scheme to a filter-based LIO system denoted as LIO-GVM. The contributions can be summarized as follows:

TABLE I  
NOTATIONS OF THIS LETTER

Notation	Explanation
$G, I, L$	The Global, IMU, and LiDAR frame
$t_k$	The end time of the $k_{th}$ LiDAR scan
$\tau_i$	The sample time of $i_{th}$ IMU input, N.B. $\tau_i \in [t_{k-1}, t_k]$
${}^G\mathbf{T}_I$	The transformation matrix of $I$ w.r.t. $G$
${}^G\mathbf{R}_I, {}^G\mathbf{p}_I$	The rotation matrix and translation vector of $I$ w.r.t. $G$
${}^{L^k}\mathbf{p}_j$	The $j_{th}$ point coordinate with reference to $L$ at time $t_k$
${}^G\mathbf{v}_i$	The coordinate of the $i_{th}$ voxel with reference to $G$
${}^G\boldsymbol{\mu}_i, {}^G\mathbf{C}_i$	The centroid vector and covariance matrix of voxel at ${}^G\mathbf{v}_i$
$[\mathbf{p}]_{\times}, \mathbf{p}^T$	The skew-symmetric matrix and transpose of vector $\mathbf{p}$

- We propose a new correspondence matching method and residual metric for filter-based LIO. This scheme is capable of handling noise introduced by low-cost IMUs by rejecting mismatched correspondences. Additionally, the metric measures not only distance but also variance disparity, which enhances the comprehensiveness and accuracy of the residual formulation.
- We propose a simple yet efficient map scheme. The map only necessitates the maintenance of the centroid and covariance matrix for each voxel. Due to the strategic design of the residual metric, the map module can achieve fast operation while maintaining the accuracy of state estimation.
- We implement the two key techniques into a filter-based LIO system and evaluate its robustness and efficiency through various experiments (see Fig. 1). To the benefit of the robotics community, our implementation code is open-sourced at [https://github.com/Ji1Xingyu/lio\\_gvm](https://github.com/Ji1Xingyu/lio_gvm).

## II. PRELIMINARY

### A. Notation

The important notations used in this letter are listed in Tab. I. Besides, we assume a static calibrated extrinsic matrix  ${}^L\mathbf{T}_I = ({}^L\mathbf{R}_I, {}^L\mathbf{p}_I)$  from IMU frame to LiDAR frame.

### B. System Description

The proposed LIO-GVM is modeled as a discrete-time dynamical system sampled at the IMU rate. Its state  $\mathbf{x}$  is defined on manifold  $\mathcal{M}$  as:

$$\mathcal{M} = SO(3) \times \mathbb{R}^{15},$$

$$\mathbf{x} \doteq [{}^G\mathbf{R}_I^T \quad {}^G\mathbf{p}_I^T \quad {}^G\mathbf{v}_I^T \quad \mathbf{b}_\omega^T \quad \mathbf{b}_a^T \quad {}^G\mathbf{g}^T]^T, \quad (1)$$

where  ${}^G\mathbf{v}_I$  and  ${}^G\mathbf{g}$  are the velocity of IMU and gravity vector with reference to the global frame,  $\mathbf{b}_\omega$  and  $\mathbf{b}_a$  are the bias vectors of gyroscope and accelerometer of the IMU. The true state  $\mathbf{x}$  of the system can be divided into two states:

$$\mathbf{x}_k = \hat{\mathbf{x}}_k \boxplus \delta\mathbf{x}_k,$$

$$\delta\mathbf{x}_k = \mathbf{x}_k \boxminus \hat{\mathbf{x}}_k$$

$$= [{}^G\delta\mathbf{r}_{I_k}^T \quad {}^G\delta\mathbf{p}_{I_k}^T \quad {}^G\delta\mathbf{v}_{I_k}^T \quad \delta\mathbf{b}_{\omega_k}^T \quad \delta\mathbf{b}_{a_k}^T \quad {}^G\delta\mathbf{g}_k^T]^T, \quad (2)$$

where  $\delta\mathbf{x}_k \in \mathbb{R}^{18}$  is the error state,  $\hat{\mathbf{x}}_k \in \mathcal{M}$  is the nominal state,  $\boxminus$  and  $\boxplus$  are encapsulated operators that represent a bijective mapping between the manifold  $\mathcal{M}$  and its local tangent

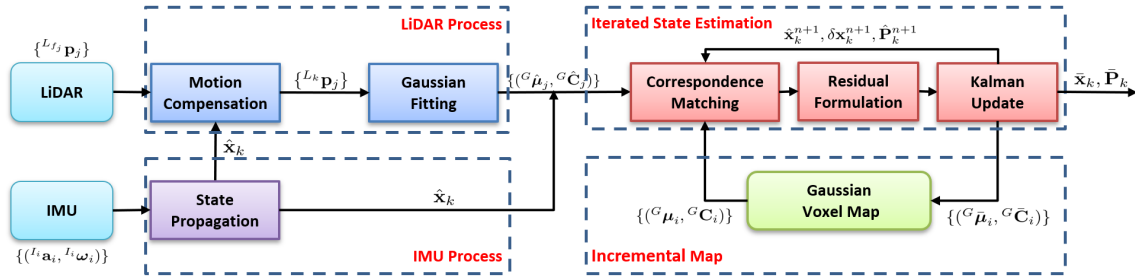


Fig. 2. System Workflow.

space  $\mathbb{R}^{18}$  [24];  ${}^G\delta\mathbf{r}_{I_k} = {}^G\mathbf{R}_{I_k} \boxminus {}^G\hat{\mathbf{R}}_I = \text{Log}({}^G\mathbf{R}_{I_k} {}^G\hat{\mathbf{R}}_I^{-1})$  is the minimal representation of the error rotation. In this way, we can use the iterative error state Kalman filter (IESKF) to estimate the error state  $\delta\mathbf{x}_k$  on Euclidean space and then project it back to the manifold using (2) for the maintenance of the true state  $\mathbf{x}_k$ .

### III. METHODOLOGY

Given the estimate of the last scan:  $\bar{\mathbf{x}}_{k-1}$  and  $\bar{\mathbf{P}}_{k-1}$ , we will detail the system workflow in the following subsections.

#### A. IMU Process

Recalling the state defined in (1), we have the following discrete model based on continuous kinematics equations [24]:

$$\mathbf{x}_{i+1} = \mathbf{x}_i \boxplus \mathbf{f}(\mathbf{x}_i, \mathbf{u}_i, \mathbf{w}_i), \quad (3)$$

where  $\mathbf{u}_i$ ,  $\mathbf{w}_i$ , and  $\mathbf{f}$  are the system input, system noise, and kinematics function respectively. Please refer to Appendix A for the detailed formulations. Firstly, the mean of the nominal state  $\hat{\mathbf{x}}_i$  will be predicted without considering the noise  $\mathbf{w}_i$ :

$$\hat{\mathbf{x}}_{i+1} = \hat{\mathbf{x}}_i \boxplus \mathbf{f}(\hat{\mathbf{x}}_i, \mathbf{u}_i, \mathbf{0}); \hat{\mathbf{x}}_0 = \bar{\mathbf{x}}_{k-1}. \quad (4)$$

Consequently, this will result in the accumulation of inaccuracies. To cope with the problem,  $\mathbf{w}_i$  is taken into account in the prediction of the error state  $\delta\mathbf{x}_i$ :

$$\delta\mathbf{x}_{i+1} \approx \mathbf{F}_{\delta\mathbf{x}}\delta\mathbf{x}_i + \mathbf{F}_{\mathbf{w}}\mathbf{w}_i; \delta\mathbf{x}_0 = \delta\bar{\mathbf{x}}_{k-1} = \mathbf{0}, \quad (5)$$

where  $\mathbf{F}_{\delta\mathbf{x}}$  and  $\mathbf{F}_{\mathbf{w}}$  are the Jacobian matrices of  $\mathbf{f}()$  w.r.t.  $\delta\mathbf{x}_i$  and  $\mathbf{w}_i$  [9]. In the implementation, the system noise  $\mathbf{w}_i$  is considered as Gaussian white noise following the normal distribution  $\mathcal{N}(\mathbf{0}, \mathbf{W})$ , where  $\mathbf{W}$  is the covariance matrix. The error state  $\delta\mathbf{x}_i$  is an independent random vector with multivariate normal distribution:  $\delta\mathbf{x}_i \sim \mathcal{N}(\mathbf{0}, \mathbf{P}_i)$ . As a consequence, the predicted covariance matrix  $\hat{\mathbf{P}}_{i+1}$  of  $\delta\mathbf{x}_{i+1}$  can be calculated as the linear transformation:

$$\hat{\mathbf{P}}_{i+1} = \mathbf{F}_{\delta\mathbf{x}}\hat{\mathbf{P}}_i\mathbf{F}_{\delta\mathbf{x}}^T + \mathbf{F}_{\mathbf{w}}\mathbf{W}\mathbf{F}_{\mathbf{w}}^T; \hat{\mathbf{P}}_0 = \bar{\mathbf{P}}_{k-1}. \quad (6)$$

The IMU process module utilizes the state estimate from the previous scan as the initial condition and recursively predicts  $\hat{\mathbf{x}}_{i+1}$ ,  $\delta\mathbf{x}_{i+1}$  and  $\hat{\mathbf{P}}_{i+1}$  till the end time of the current LiDAR scan  $t_k$ .

#### B. LiDAR Process

All the LiDAR points  ${}^{L_j}\mathbf{p}_j$  with timestamps  $\gamma_j \in [t_{k-1}, t_k]$  are cached to form a point cloud  $\mathcal{P}_k$ . For most commercial LiDAR, the points are sampled under different timestamps, which will introduce motion distortion to the cloud  $\mathcal{P}_k$ . We seek to compensate for the distortion by projecting all the points in  $\mathcal{P}_k$  to  $L_k$ , the LiDAR frame at  $t_k$ . To this end, we adopt the backward propagation proposed in [8] to obtain the relative motion between IMU frames sampled at  $\gamma_j$  and  $t_k$ :  ${}^{I_k}\mathbf{T}_{I_j}$ . The point  ${}^{L_j}\mathbf{p}_j$  can thus be projected to  $L_k$  as:

$${}^{L_k}\mathbf{p}_j = {}^{I}T_L^{-1}{}^{I_k}\mathbf{T}_{I_j}{}^{I}T_L{}^{L_j}\mathbf{p}_j. \quad (7)$$

Moreover, a representative descriptor for the point is required for robust correspondence matching. Thus, we represent the deskewed points as a collection of Gaussian distributions. For each point  ${}^{L_k}\mathbf{p}_j$ , we collect its nearest  $y$  neighbors and fit them to a Gaussian distribution  $\mathcal{N}({}^{L_k}\boldsymbol{\mu}_j, {}^{L_k}\mathbf{C}_j)$  [14]. Eventually, the LiDAR process module outputs a collection of the fitted Gaussian distributions for all the points:  $\{{}^{L_k}\boldsymbol{\mu}_j, {}^{L_k}\mathbf{C}_j\}$ .

#### C. Iterated State Estimation

Upon completion of the IMU and LiDAR processes, the following steps for the IESKF-based LIO system involve correspondence matching, residual formulation, and Kalman update. However, the majority of existing filter-based LIO systems [4], [6], [8] typically adopt a straightforward strategy for correspondence matching, that is, matching the point  ${}^{L_k}\mathbf{p}_j$  in the input LiDAR scan with its nearest feature within the target map and treating the ensuing point-to-feature distance as the residual. This strategy involves projecting  ${}^{L_k}\mathbf{p}_j$  to the global frame as:

$${}^G\hat{\mathbf{P}}_j = {}^G\hat{\mathbf{T}}_{I_k}{}^{I}T_L{}^{L_k}\mathbf{p}_j = {}^G\hat{\mathbf{T}}_{I_{k-1}}{}^{I_{k-1}}\hat{\mathbf{T}}_{I_k}{}^{I}T_L{}^{L_k}\mathbf{p}_j. \quad (8)$$

For long-term odometry, the inevitable accumulation of localization drifts introduces errors to  ${}^G\hat{\mathbf{T}}_{I_{k-1}}$ . Simultaneously, the presence of spike noise, a common issue in low-cost IMUs, leads to inaccuracies in  ${}^{I_{k-1}}\hat{\mathbf{T}}_{I_k}$ . These factors prevent  ${}^{L_k}\mathbf{p}_j$  from being projected to its exact corresponding feature, generating mismatches (see Fig. 3). Besides, matching the nearest feature in the map could be computationally intensive if the map size grows too large in long-term odometry. To cope with these issues, we propose a new residual formulation for IESKF, which can mitigate incorrectly matched correspondences while maintaining computational efficiency (see Fig. 3). The details are described in the following subsections.

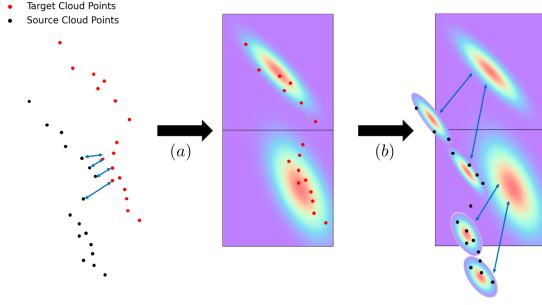


Fig. 3. Directly registering the source points to the nearest target points would generate mismatches (shown in the left image). Instead, we: (a). Voxelize the target cloud and fit the points within each voxel as a Gaussian distribution. (b). Fit each source point as a Gaussian distribution and match it with the near & similar target distributions.

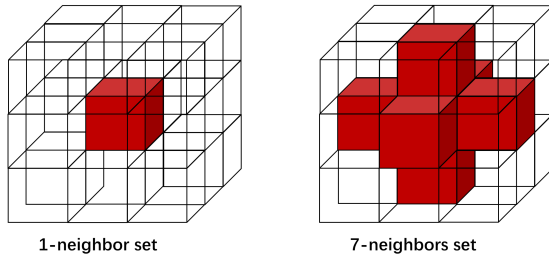


Fig. 4. The different neighbor set  $\mathcal{V}_j$  of a given voxel  ${}^G\mathbf{v}_j^n$ .

1) *Correspondence Matching*: Suppose the iterated state estimation module is under the  $n_{th}$  iteration and the corresponding state estimation is  $\hat{\mathbf{x}}_k^n, \delta\mathbf{x}_k^n$ . We first project the fitted distributions into the global frame as:

$$\begin{aligned} {}^G\hat{\boldsymbol{\mu}}_j^n &= {}^G\hat{\mathbf{T}}_{L_k}^n L_k \boldsymbol{\mu}_j, \\ {}^G\hat{\mathbf{C}}_j^n &= {}^G\hat{\mathbf{R}}_{L_k}^n L_k \mathbf{C}_j {}^G\hat{\mathbf{T}}_{L_k}^{nT}. \end{aligned} \quad (9)$$

For each projected distribution  $({}^G\hat{\boldsymbol{\mu}}_j^n, {}^G\hat{\mathbf{C}}_j^n)$ , we aim to find its near and similar correspondence in the global voxel map. Each voxel contains one Gaussian distribution  $({}^G\boldsymbol{\mu}_i, {}^G\mathbf{C}_i)$  (details of the global map is presented in Section III-D). Hellinger distance is a statistical measure that quantifies the divergence between two probability distributions. Its value is dominated by two terms: a similarity term and a distance term. The similarity term captures the resemblance between two probability distributions, while the distance term quantifies the separation. For the correspondence evaluation, we extract the similarity term from the squared Hellinger distance [25] and denote it as the similarity metric  $s_{j,i}$ :

$$s_{j,i} = \sqrt{\frac{(\det \mathbf{C}_j \det \mathbf{C}_i)^{1/2}}{\det (\mathbf{C}_j/2 + \mathbf{C}_i/2)}}. \quad (10)$$

The larger the  $s_{j,i}$  is, the more similar the two distributions are. The correspondence matching procedure can now be conceptualized as follows: We first find the voxel coordinate  ${}^G\mathbf{v}_j^n$  in the global map in which  ${}^G\hat{\boldsymbol{\mu}}_j^n$  occupies. Then, we define a neighbor set of the occupied voxel as  $\mathcal{V}_j$  (the selection for  $\mathcal{V}_j$  in implementation is illustrated in Fig. 4). After that, we calculate the similarity  $s_{j,i}$  for all the voxels in  $\mathcal{V}_j$  and

discard the voxel pairs  $({}^G\mathbf{v}_j^n, {}^G\mathbf{v}_i)$  with the similarity smaller than a threshold  $s_t$ . The rest voxel pairs, deemed as effective correspondences, will be utilized for the residual formulation.

2) *Residual Formulation*: Before presenting the new residual metric, it is necessary to explain the observation model and state estimation scheme for IESKF. This will provide the rationale behind the proposed residual metric. The observation function of the system is:

$$\mathbf{z}_k^n = \mathbf{h}(\hat{\mathbf{x}}_k^n \boxplus \delta\mathbf{x}_k^n) + \mathbf{v}_k, \quad (11)$$

where  $\mathbf{v}_k$  is the measurement noise satisfying  $\mathbf{v}_k \sim n(0, \mathbf{V}_k)$ ,  $\mathbf{h}(\cdot)$  is the observation function that maps the state space to the observation space. Since the error state is quite small, we can linearize the observation at  $\hat{\mathbf{x}}_k^n$ :

$$\mathbf{z}_k^n \approx \mathbf{h}(\hat{\mathbf{x}}_k^n) + \mathbf{H}^n \delta\mathbf{x}_k^n + \mathbf{v}_k, \quad (12)$$

where  $\mathbf{H}^n$  is the Jacobian matrix of  $\mathbf{h}(\hat{\mathbf{x}}_k^n \boxplus \delta\mathbf{x}_k^n)$  w.r.t.  $\delta\mathbf{x}_k^n$ . As  $\delta\mathbf{x}_k$  and  $\delta\mathbf{x}_k^n$  lie in different tangent space of the manifold  $\mathcal{M}$  (the tangent space of  $\hat{\mathbf{x}}_k$  and  $\hat{\mathbf{x}}_k^n$  respectively), we need to project  $\delta\mathbf{x}_k$  to  $\delta\mathbf{x}_k^n$  in the tangent space as:

$$\delta\mathbf{x}_k = (\hat{\mathbf{x}}_k^n \boxplus \delta\mathbf{x}_k^n) \boxminus \hat{\mathbf{x}}_k = \hat{\mathbf{x}}_k^n \boxminus \hat{\mathbf{x}}_k + (\mathbf{J}^n)^{-1} \delta\mathbf{x}_k^n, \quad (13)$$

where  $\mathbf{J}^n$  is the inverse of the Jacobian matrix of  $(\hat{\mathbf{x}}_k^n \boxplus \delta\mathbf{x}_k^n) \boxminus \hat{\mathbf{x}}_k$  w.r.t.  $\mathbf{x}_k^n$ . Readers may refer to Appendix A for the detailed formulation of  $\mathbf{J}^n$ . Combining (12) and (13), following the Bayesian rule, we have the maximum a posteriori (MAP) problem:

$$\delta\mathbf{x}_k^n = \arg \min_{\delta\mathbf{x}_k^n} \left( \|\delta\mathbf{x}_k\|_{\mathbf{P}^{-1}}^2 + \|\mathbf{h}(\hat{\mathbf{x}}_k^n) + \mathbf{H}^n \delta\mathbf{x}_k^n\|_{\mathbf{V}_k^{-1}}^2 \right). \quad (14)$$

Given that the matched correspondences are Gaussian distribution pairs, we aim to design a residual metric such that the second term in (14) can represent both the distance and the variance disparity. Let's consider the weighted Mahalanobis distance presented as follows:

$$\begin{aligned} \|\mathbf{h}(\mathbf{x}_k)\|_{\mathbf{V}_k^{-1}}^2 &= \\ \sum_{j=0}^m (s_{j,i}^n)^2 ({}^G\hat{\boldsymbol{\mu}}_j^n - {}^G\boldsymbol{\mu}_i)^T (\hat{\mathbf{C}}_j^n + \mathbf{C}_i)^{-1} ({}^G\hat{\boldsymbol{\mu}}_j^n - {}^G\boldsymbol{\mu}_i), \end{aligned} \quad (15)$$

where  $m$  is the number of matched correspondences. The Mahalanobis distance is weighted by the similarity of the matched correspondences, ensuring that the pairs with higher similarity and closer distance contribute more to the estimation process, which aligns with our objective. Adopting this formula, the resulting residual metric for  $({}^G\hat{\boldsymbol{\mu}}_j^n, {}^G\hat{\mathbf{C}}_j^n)$  would be:

$$\mathbf{z}_{k,j}^n = s_{j,i}^n \mathbf{D}_j ({}^G\hat{\boldsymbol{\mu}}_j^n - {}^G\boldsymbol{\mu}_i). \quad (16)$$

Please refer to Appendix B for the detailed derivation and definition.

3) *State Update*: The Jacobian matrix  $\mathbf{H}_{k,j}^n$  of  $\mathbf{z}_{k,j}^n$  w.r.t.  $\delta\mathbf{x}_k^n$  is:

$$\mathbf{H}_{k,j}^n = \begin{bmatrix} -s_j \mathbf{D}_j [{}^I\mathbf{q}_j]_{\times} & s_j \mathbf{D}_j & \mathbf{0}_{3 \times 15} \end{bmatrix}. \quad (17)$$

Please refer to Appendix C for the derivation and definition details. With the Jacobian matrix, the optimal solution of the MAP problem (14) can be solved by the Kalman update [26]. Readers may refer to Appendix A for the specific procedures.

### D. Incremental Global Map

The global map is composed of voxels stored as a hash table:  $\mathbb{Z}^3 \rightarrow \mathbb{R}^3 \times \mathbb{R}^{3 \times 3}$ , which builds a map from the voxel coordinate  ${}^G\mathbf{v}_i$  to its centroid  ${}^G\boldsymbol{\mu}_i$  and the covariance matrix  ${}^G\mathbf{C}_i$ . This structure demonstrates significant efficiency in querying, achieving an optimal  $\mathcal{O}(1)$  time complexity for correspondence matching.

The initialization of the global map is similar to the operation in [16]. The first scan is regarded as the global frame  $G = L_0$ . Each point in the scan is subsequently fitted to a Gaussian distribution as the procedure in III-B to obtain  $({}^G\hat{\mathbf{p}}_j, \mathbf{C}_j)$ . Consequently, the scan is voxelized with voxel size  $r$ . Suppose we have the voxel with coordinate  ${}^G\mathbf{v}_i$  encompassing a set of points  $\{{}^G\mathbf{p}_m\}$ , the centroid and covariance matrix  ${}^G\boldsymbol{\mu}_i, {}^G\mathbf{C}_i$  will be calculated as the average of the distributions within. Once the current estimate  $\bar{\mathbf{x}}_k$  is acquired, the current scan contributes to the global map. Since the projected Gaussian distributions have been obtained during the state estimation phase, we proceed to voxelize the current scan following (18), resulting in a temporary voxel map  ${}^G\mathbf{v}_j \rightarrow (\bar{\boldsymbol{\mu}}_j, \bar{\mathbf{C}}_j)$ . For each voxel present in this temporary voxel map, we query its coordinate  ${}^G\mathbf{v}_j$  in the global map. If the global map doesn't contain the voxel, we directly insert the voxel into the global map. This operation is time-efficient since the insert operation for a hash table has a time complexity of  $\mathcal{O}(1)$ . Otherwise, the global map will be updated as:

$$\begin{aligned} {}^G\boldsymbol{\mu}_j &= \frac{M^G\boldsymbol{\mu}_j + N^G\bar{\boldsymbol{\mu}}_j}{M + N}, \\ {}^G\mathbf{C}_j &= \frac{M^G\mathbf{C}_j + N^G\bar{\mathbf{C}}_j}{M + N}, \\ M &= \max(M, N), \end{aligned} \quad (18)$$

where  $M$  is the recorded point number of voxel  ${}^G\mathbf{v}_j$  in the global map,  $N$  is the corresponding one in the temporary voxel map. In this way, the global map only necessitates the maintenance of the centroid and covariance matrix for each voxel, which is considerably efficient in terms of memory usage and time efficiency compared to maintaining a tree structure storing all points [9] or embedding additional structures into the voxels [4], [23]. Consequently, this enables an incremental update of the global map without the necessity to delete voxels from the map.

## IV. EXPERIMENT

In this section, the proposed system will be evaluated in terms of accuracy, temporal efficiency, and storage efficiency. All the experiments are conducted on a laptop with a 2.3 GHz AMD Ryzen 7 6800H CPU and 16 GB RAM. We totally choose 9 sequences from two representative datasets for the evaluation. The first 5 sequences, denoted as **nc\_\***, are selected from Newer College dataset [27], with an OS1-64 LiDAR at a scan rate of 10Hz and a built-in 6-axis IMU sampled at 100Hz. The rest sequences are selected from the MCD VIRAL dataset [28], collected by an OS1-128 LiDAR sampled at 10Hz, a Livox Mid-70 LiDAR, and a VectorNav VN100 9-axis IMU sampled at 800 Hz. In order to evaluate the influence of IMU on the odometry accuracy, we perform

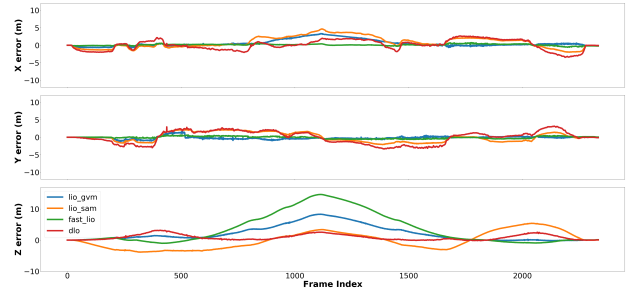


Fig. 5. The position error of different methods on sequence ntu\_13. We find that the position error is most significant along the z axis, due to the severe elevation changes.

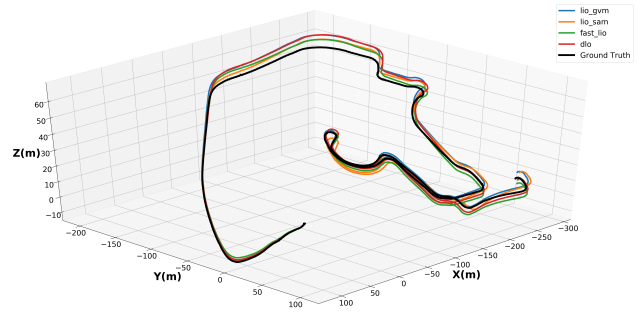


Fig. 6. The trajectories reference to the ground on sequence ntu\_04.

experiments on different IMUs for the same sequences from MCD VIRAL dataset: **ntu\_\*** denoting OS1-128 LiDAR with VN100 IMU, **ntuo\_\*** denoting OS1-128 LiDAR with its built-in IMU. The ground truth poses for both datasets are generated by registering each LiDAR scan to a highly accurate prior map using an ICP method.

### A. Evaluation of Odometry Accuracy

The accuracy of odometry is evaluated by comparing the KITTI metric [29]: the average translation error (ATE), and the average rotation error (ARE). We compare LIO-GVM with three state-of-the-art LiDAR (-inertial) odometry algorithms: DLO [30], LIO-SAM [1], and FAST-LIO2 [9]. DLO is a GICP-based LO while LIO-SAM and FAST-LIO2 are LIO systems. It should be noted that no loop closures were performed for all the methods.

Two variations of the proposed system denoted as LIO-GVM(w/o s) and LIO-GVM(plane) are tested for ablation study. LIO-GVM(w/o s) is implemented without the outlier rejecting scheme proposed in Sec. III-C1. LIO-GVM(plane) replaces the proposed new residual metric with the point-to-plane distance [9]. As shown in Tab. II, both LIO-GVM(w/o s) and LIO-GVM(plane) turn worse compared to the original system for all the sequences, indicating that the proposed correspondence matching scheme and residual metric both contribute to the accuracy of the system. The accuracy of LIO-GVM(w/o s) tends to be much worse than LIO-GVM(plane), which is because the residual metric inherently reduces the weights for mismatches.

As illustrated in Tab. II, LIO-GVM achieves the best results for most sequences. Note that LIO-SAM is not applicable

TABLE II  
EVALUATION AND COMPARISON OF ODOMETRY ACCURACY ON ALL THE SEQUENCES

	ntu_02	ntu_04	ntu_10	ntu_13	ntuo_02	ntuo_04	ntuo_10	ntuo_13	nc_01	nc_02	nc_05	nc_06	nc_07
DLO	6.46/0.43	3.65/0.11	7.65/0.51	3.98/0.20	6.46/0.43	3.75/0.11	7.65/0.51	<u>3.98/0.20</u>	4.20/0.51	4.27/0.37	3.44/0.44	1.31/0.62	1.73/0.18
LIO-SAM	7.80/0.52	3.71/0.23	9.32/0.63	3.05/0.16	- <sup>a</sup>	-	-	-	-	-	-	-	-
FAST-LIO2	2.09/0.24	<b>2.11/0.13</b>	<b>2.34/0.15</b>	2.89/0.11	5.64/0.80	3.51/0.23	<u>7.32/0.41</u>	6.79/0.50	<u>3.23/0.37</u>	4.15/0.43	<b>3.13/0.26</b>	<u>0.94/0.37</u>	<u>1.16/0.15</u>
LIO-GVM(w/o s)	2.37/0.40	2.35/0.11	3.21/0.14	2.79/0.14	5.51/0.68	4.73/0.39	6.59/0.39	4.58/0.26	3.36/0.31	4.76/0.44	3.46/0.47	1.28/0.43	1.38/0.20
LIO-GVM(plane)	8.24/0.68	6.91/0.41	8.29/0.74	5.77/0.43	9.34/0.90	7.95/0.54	10.2/0.81	8.89/0.73	6.29/0.49	6.30/0.67	4.54/0.72	2.48/0.59	3.45/0.30
LIO-GVM	<b>1.74/0.46</b>	<b>2.26/0.05</b>	<b>3.16/0.11</b>	<b>2.74/0.09</b>	<b>3.23/0.40</b>	<b>2.69/0.14</b>	<b>4.25/0.27</b>	<b>3.60/0.18</b>	<b>2.47/0.26</b>	<b>3.20/0.35</b>	<u>3.27/0.33</u>	<b>0.89/0.33</b>	<b>1.10/0.17</b>

The errors are represented as ATE[%]/ARE[deg/10m] (the smaller the better). Parameters for all methods are kept constant across sequences for consistency. We only align the position and orientation of the sequences at the origin for a comprehensive evaluation.

**Bold** value stands for the best value; underline value stands for the second best value; '-' denotes that the algorithm is not applicable.

<sup>a</sup> The built-in IMU of OS1-128 and OS1-64 cannot provide the attitude data for LIO-SAM. Thus, LIO-SAM is not available for these sequences.

TABLE III  
EVALUATION OF THE TEMPORAL EFFICIENCY IN SEQUENCES ON MAPPING PROCEDURES

	Gaussian Fitting		Correspondence Match		Incremental Update		Total Map Time	
	ikd-Tree	GVM	ikd-Tree	GVM	ikd-Tree	GVM	ikd-Tree	GVM
ntu_02	<b>0</b>	11.61	25.05	<b>1.29</b>	<b>2.45</b>	5.13	27.50	<b>18.03</b>
ntu_04	<b>0</b>	12.91	24.26	<b>1.41</b>	<b>3.96</b>	5.34	28.22	<b>19.66</b>
ntu_10	<b>0</b>	11.86	24.27	<b>1.34</b>	<b>3.97</b>	5.87	28.24	<b>19.08</b>
ntu_13	<b>0</b>	12.71	24.89	<b>1.67</b>	<b>3.62</b>	5.18	28.51	<b>19.56</b>
nc_01	<b>0</b>	8.10	14.36	<b>0.69</b>	<b>0.78</b>	2.97	15.14	<b>11.76</b>
nc_02	<b>0</b>	8.25	15.76	<b>0.73</b>	<b>0.92</b>	2.84	16.68	<b>11.82</b>
nc_05	<b>0</b>	7.73	12.62	<b>0.67</b>	<b>0.57</b>	2.84	13.19	<b>11.24</b>
nc_06	<b>0</b>	7.19	13.66	<b>0.70</b>	<b>0.81</b>	3.23	14.47	<b>11.12</b>
nc_07	<b>0</b>	8.99	15.67	<b>0.62</b>	<b>1.11</b>	3.18	16.78	<b>12.79</b>

We evaluate the average time consumed per scan [ms].

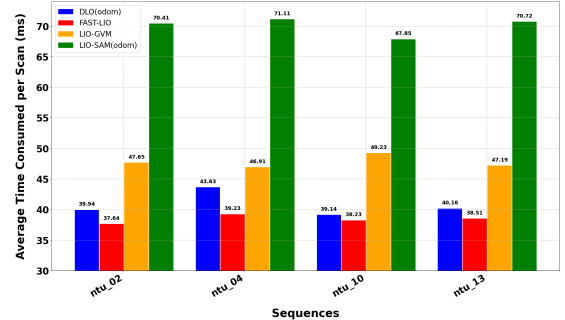
**Bold** value stands for the best value.

for **ntuo**\* and **nc**\* sequences as it requires the equipment of a 9-axis IMU. The performance of all LIO systems is negatively impacted in **ntuo**\* compared to **ntu**\* sequences due to the equipment of a low-cost IMU. Nevertheless, LIO-GVM is able to mitigate the impact of IMU noises through its proposed correspondence matching scheme, which can reject outlier correspondences. Additionally, LIO-GVM incorporates a new residual metric that takes similarity into account during the estimation phase, allowing more effective correspondences to have a greater influence on the estimation. Consequently, LIO-GVM exhibits the best accuracy compared to other LIO systems. However, all the methods have a common limitation in accommodating the pronounced changes in elevation in the **ntu**\* sequences, as seen in Fig. 6 and Fig. 5.

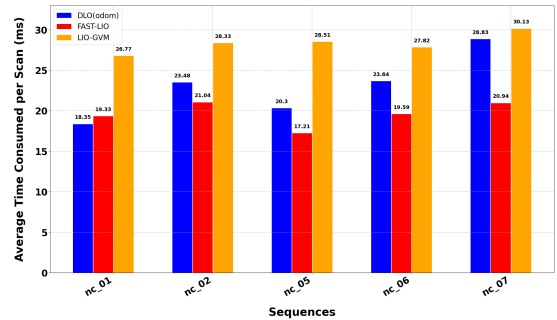
Overall, LIO-GVM has demonstrated the best performance regarding odometry accuracy, showing the effectiveness of the error-rejecting correspondence matching scheme and the distribution-based residual formulation in achieving precise location estimation across various sensor setups, especially in long-term applications or with cheaper IMUs.

### B. Evaluation of Storage Efficiency

In this section, we evaluate the storage consumption of the global map generated by LIO-GVM. Specifically, in LIO-GVM, we have defined a custom point type using the Point Cloud Library (PCL). Each point encapsulates all the elements of  $(\mu_i, C_i, M)$ , comprising a total of four integer values and nine floating-point values. All the voxels are stored in a compressed binary .pcd file. For other systems, we configure their local map size to be 500m, ensuring coverage of all areas within the two datasets, and save all the points in the map to a compressed binary .pcd file.



(a) MCD\_VIRAL dataset.



(b) Newer College dataset.

Fig. 7. The average time consumed per scan (ms) for all methods in different datasets.

As illustrated in Tab. IV, the map storage consumption of LIO-GVM outperforms other systems for all the sequences. This is because other systems need to ensure that the down-sampling filter of the map is not excessively large (usually  $< 0.5m$ ) to preserve the geometric information of the points. In contrast, our approach allows us to allocate a considerably

TABLE IV  
THE CONSTRUCTED MAP STORAGE ANALYSIS

	ntu_02	ntu_04	ntu_10	ntu_13	nc_01	nc_02	nc_05	nc_06	nc_07
FAST-LIO2	6.07	21.83	19.13	22.19	7.93	9.24	1.15	0.65	5.62
LIO-GVM	<b>3.55</b>	<b>12.61</b>	<b>11.39</b>	<b>8.29</b>	<b>4.25</b>	<b>4.60</b>	<b>0.13</b>	<b>0.48</b>	<b>3.01</b>

The map storage is analyzed by evaluating the **storage consumption [MB]**. All the maps are saved as binary compressed PCD files. **Bold** value stands for the best value.

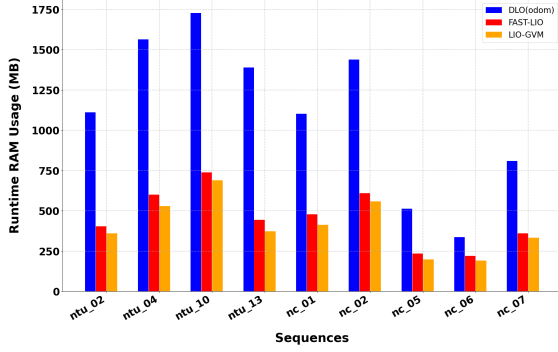


Fig. 8. The eventual runtime RAM usage for all the methods.

larger voxel size (commonly  $> 1\text{m}$ ) compared to other systems while still offering a comprehensive representation of the intra-voxel point distribution.

### C. Evaluation of Time Consumption

In this section, we will evaluate the temporal efficiency of LIO-GVM, utilizing the same parameters as those deployed in our previous odometry evaluations for consistency. We first analyze the influence of the data structure on the mapping procedure, which involves correspondence matching and incremental updates. Given the superior performance of the ikd-Tree provided in [9] compared to other dynamic tree-based structures, our comparison will be limited to this structure. While the Gaussian fitting process does not directly participate in the mapping procedure, its time consumption is still accounted for in LIO-GVM for a fair comparison. We denote the data structure in LIO-GVM for the mapping procedure as GVM. The results are illustrated in Tab. III. GVM significantly outperforms ikd-Tree in correspondence matching because the time complexity of  $k$ -nearest neighbors searching for ikd-Tree is  $\mathcal{O}(\log(n))$ , where  $n$  is the tree size; but for GVM, managed in a hash table, the corresponding time complexity is  $\mathcal{O}(1)$ . ikd-Tree slightly performs better in the incremental update. Nonetheless, GVM demonstrates superior performance in total map time.

In Fig. 7, we illustrate the average total time consumed per scan for all the sequences. The total time we evaluated includes all the procedures: data processing, pose estimation, and map update. Since LIO-SAM and DLO run map update in different thread with the pose estimation thread, we only evaluate their time consumed for state estimation. Even though the mapping procedure of LIO-GVM is faster than FAST-LIO2, FAST-LIO2 achieves the shortest total time for almost all the sequences. One possible reason is that LIO-GVM requires more geometric information from the input scan, leading to a higher-

dimensional measurement matrix. However, as illustrated in Tab. 8, the fast performance of FAST-LIO2 and DLO comes with the trade-off of increased runtime RAM usage, while LIO-GVM can achieve comparable temporal efficiency with lower RAM usage.

## V. CONCLUSION

In conclusion, this letter proposes an accurate filter-based LIO system denoted as LIO-GVM, which models the points as Gaussian distributions for robust correspondence matching. The key innovation of the system is the proposed new residual metric. Unlike previous methods that solely measure distance, our approach incorporates variance disparity, thereby enhancing the system's performance. Benefiting from the new metric, the map of LIO-GVM can be maintained in a simple yet efficient manner. We demonstrate the reliability and efficiency of LIO-GVM through extensive experiments on different datasets.

The limitation of LIO-GVM is that it requires equipment with higher resolution LiDAR to ensure informative Gaussian fitting of the input scan. Additionally, the voxel size is not adaptive to the environment. To address these limitations, future work will focus on developing an adaptive voxel representation scheme for the global map.

## APPENDIX

### A. Supplemental Material

We provide the detailed formulation of the involved matrices in the supplemental material: supplemental\_material.pdf.

### B. Derivation of the Proposed Residual Metric

Let's denote  $({}^G\hat{\boldsymbol{\mu}}_j^n - {}^G\boldsymbol{\mu}_i)$  as  ${}^G\tilde{\boldsymbol{\mu}}$ , then equate (15) with the second term in MAP problem, we'll have:

$$\|\mathbf{z}_k^n\|_{\mathbf{V}_k^{-1}}^2 = \sum_{j=0}^m (s_{j,i}^n)^{2G} \tilde{\boldsymbol{\mu}}^T (\hat{\mathbf{C}}_j^n + \mathbf{C}_i)^{-1G} \tilde{\boldsymbol{\mu}}. \quad (19)$$

Performing SVD on  $(\hat{\mathbf{C}}_j^n + \mathbf{C}_i)^{-1}$  results in  $(\hat{\mathbf{C}}_j^n + \mathbf{C}_i)^{-1} = (\mathbf{U}_j^n)^T (\boldsymbol{\Lambda}_j^n)^{-1} \mathbf{U}_j^n$ . Similarly, perform SVD on  $(\boldsymbol{\Lambda}_j^n)^{-1}$  then we have  $(\boldsymbol{\Lambda}_j^n)^{-1} = (\mathbf{Q}_j^n)^T \mathbf{V}_k^{-1} \mathbf{Q}_j^n$ . Thus,

$$\begin{aligned} (19) &= \sum_{j=0}^m (s_{j,i}^n)^{2G} \tilde{\boldsymbol{\mu}}^T (\hat{\mathbf{C}}_j^n + \mathbf{C}_i)^{-1G} \tilde{\boldsymbol{\mu}} \\ &= \sum_{j=0}^m s_{j,i}^n {}^G\tilde{\boldsymbol{\mu}}^T (\mathbf{U}_j^n)^T (\mathbf{Q}_j^n)^T \mathbf{V}_k^{-1} s_{j,i}^n \mathbf{Q}_j^n \mathbf{U}_j^n {}^G\tilde{\boldsymbol{\mu}} \quad (20) \\ &= \sum_{j=0}^m (\mathbf{z}_{k,j}^n)^T \mathbf{V}_k^{-1} \mathbf{z}_{k,j}^n, \end{aligned}$$

where:

$$\begin{aligned} \mathbf{z}_{k,j}^n &= s_{j,i}^n \mathbf{D}_j^n ({}^G \hat{\boldsymbol{\mu}}_j^n - {}^G \boldsymbol{\mu}_i), \\ \mathbf{D}_j^n &= \mathbf{Q}_j^n \mathbf{U}_j^n. \end{aligned} \quad (21)$$

### C. Derivation of Jacobian Matrix

The Jacobian matrix is given by:

$$\mathbf{H}_j^n = \frac{\partial \mathbf{z}_j(\hat{\mathbf{x}}_k \boxplus \delta \mathbf{x}_k^n, {}^L \mathbf{p}_j)}{\partial \delta \mathbf{x}_k^n} \quad (22)$$

and the observation function is:

$$\mathbf{z}_j(\hat{\mathbf{x}}_k \boxplus \delta \mathbf{x}_k^n, {}^L \mathbf{p}_j) = s_{j,i}^n \mathbf{D}_j^n ({}^G \hat{\mathbf{p}}_j - {}^G \boldsymbol{\mu}_i) \quad (23)$$

The calculation of the derivative of  $s_{j,i}^n \mathbf{D}_j^n$  w.r.t.  $\delta \mathbf{x}_k^n$  is quite comprehensive and impractical. We assume  $s_{j,i}^n \mathbf{D}_j^n$  as constant for each iteration and update its value after the iteration in the implementation. Let's pre-process the observation function:

$$\begin{aligned} \mathbf{z}_j(\hat{\mathbf{x}}_k \boxplus \delta \mathbf{x}_k^n, {}^L \mathbf{p}_j) &= s_j \mathbf{D}_j^n \left( {}^G \hat{\mathbf{p}}_{I_k} + {}^G \delta \mathbf{p}_{I_k} - {}^G \boldsymbol{\mu}_j \right. \\ &\quad \left. + {}^G \hat{\mathbf{R}}_{I_k} \text{Exp}({}^G \delta \mathbf{r}_{I_k}) ({}^I \mathbf{R}_{L_k} {}^L \mathbf{p}_j + {}^I \mathbf{p}_{L_k}) \right). \end{aligned} \quad (24)$$

Due to the minute transformation between two LiDAR frames, we have:

$$\text{Exp}({}^G \delta \mathbf{r}_{I_k}) \approx \mathbf{I} + [{}^G \delta \mathbf{r}_{I_k}]_{\times}. \quad (25)$$

Combining (24) and (25) leads to:

$$\begin{aligned} \mathbf{z}_j(\hat{\mathbf{x}}_k \boxplus \delta \mathbf{x}_k^n, {}^L \mathbf{p}_j) &= s_j \mathbf{D}_j^n \left( {}^G \hat{\mathbf{p}}_{I_k} + {}^G \delta \mathbf{p}_{I_k} - {}^G \boldsymbol{\mu}_j \right. \\ &\quad \left. + {}^G \hat{\mathbf{R}}_{I_k} {}^I \mathbf{q}_j - {}^G \hat{\mathbf{R}}_{I_k} [{}^I \mathbf{q}_j]_{\times} {}^G \delta \mathbf{r}_{I_k} \right), \end{aligned} \quad (26)$$

where  ${}^I \mathbf{q}_j = {}^I \mathbf{R}_{L_k} {}^L \mathbf{p}_j + {}^I \mathbf{p}_{L_k}$ . Recalling (22), it is easy to derive the Jacobian matrix  $\mathbf{H}_j^n$  as following:

$$\mathbf{H}_j^n = \begin{bmatrix} -s_j \mathbf{D}_j^n [{}^I \mathbf{q}_j]_{\times} & s_j \mathbf{D}_j^n & \mathbf{0}_{3 \times 15} \end{bmatrix} \quad (27)$$

### REFERENCES

- [1] T. Shan, B. Englot, D. Meyers, W. Wang, C. Ratti, and D. Rus, "Lio-sam: Tightly-coupled lidar inertial odometry via smoothing and mapping," in *2020 IEEE/RSJ international conference on intelligent robots and systems (IROS)*. IEEE, 2020, pp. 5135–5142.
- [2] T.-M. Nguyen, D. Duberg, P. Jensfelt, S. Yuan, and L. Xie, "Slic: Multi-input multi-scale surfel-based lidar-inertial continuous-time odometry and mapping," *IEEE Robotics and Automation Letters*, vol. 8, no. 4, pp. 2102–2109, 2023.
- [3] H. Ye, Y. Chen, and M. Liu, "Tightly coupled 3d lidar inertial odometry and mapping," in *2019 International Conference on Robotics and Automation (ICRA)*. IEEE, 2019, pp. 3144–3150.
- [4] C. Bai, T. Xiao, Y. Chen, H. Wang, F. Zhang, and X. Gao, "Faster-lio: Lightweight tightly coupled lidar-inertial odometry using parallel sparse incremental voxels," *IEEE Robotics and Automation Letters*, vol. 7, no. 2, pp. 4861–4868, 2022.
- [5] C. Yuan, W. Xu, X. Liu, X. Hong, and F. Zhang, "Efficient and probabilistic adaptive voxel mapping for accurate online lidar odometry," *IEEE Robotics and Automation Letters*, vol. 7, no. 3, pp. 8518–8525, 2022.
- [6] C. Qin, H. Ye, C. E. Pranata, J. Han, S. Zhang, and M. Liu, "Lins: A lidar-inertial state estimator for robust and efficient navigation," in *2020 IEEE international conference on robotics and automation (ICRA)*. IEEE, 2020, pp. 8899–8906.
- [7] S. A. Ludwig, "Investigation of orientation estimation of multiple imus," *Unmanned Systems*, vol. 9, no. 04, pp. 283–291, 2021.
- [8] W. Xu and F. Zhang, "Fast-lio: A fast, robust lidar-inertial odometry package by tightly-coupled iterated kalman filter," *IEEE Robotics and Automation Letters*, vol. 6, no. 2, pp. 3317–3324, 2021.
- [9] W. Xu, Y. Cai, D. He, J. Lin, and F. Zhang, "Fast-lio2: Fast direct lidar-inertial odometry," *IEEE Transactions on Robotics*, vol. 38, no. 4, pp. 2053–2073, 2022.
- [10] S. Yuan, H. Wang, and L. Xie, "Survey on localization systems and algorithms for unmanned systems," *Unmanned Systems*, vol. 9, no. 02, pp. 129–163, 2021.
- [11] J. Zhang and S. Singh, "Loam: Lidar odometry and mapping in real-time," in *Robotics: Science and Systems*, vol. 2, no. 9. Berkeley, CA, 2014, pp. 1–9.
- [12] Y. Pan, P. Xiao, Y. He, Z. Shao, and Z. Li, "Mulls: Versatile lidar slam via multi-metric linear least square," in *2021 IEEE International Conference on Robotics and Automation (ICRA)*. IEEE, 2021, pp. 11 633–11 640.
- [13] J. Behley and C. Stachniss, "Efficient surfel-based slam using 3d laser range data in urban environments," in *Robotics: Science and Systems*, vol. 2018, 2018, p. 59.
- [14] P. Biber and W. Straßer, "The normal distributions transform: A new approach to laser scan matching," in *Proceedings 2003 IEEE/RSJ International Conference on Intelligent Robots and Systems (IROS 2003)(Cat. No. 03CH37453)*, vol. 3. IEEE, 2003, pp. 2743–2748.
- [15] A. Segal, D. Haehnel, and S. Thrun, "Generalized-icp," in *Robotics: science and systems*, vol. 2, no. 4. Seattle, WA, 2009, p. 435.
- [16] K. Koide, M. Yokozuka, S. Oishi, and A. Banno, "Voxelized gicp for fast and accurate 3d point cloud registration," in *2021 IEEE International Conference on Robotics and Automation (ICRA)*. IEEE, 2021, pp. 11 054–11 059.
- [17] M. Yokozuka, K. Koide, S. Oishi, and A. Banno, "Litamin2: Ultra light lidar-based slam using geometric approximation applied with kl-divergence," in *2021 IEEE International Conference on Robotics and Automation (ICRA)*. IEEE, 2021, pp. 11 619–11 625.
- [18] Y. Liang, S. Müller, D. Schwendner, D. Rolle, D. Ganesch, and I. Schaffer, "A scalable framework for robust vehicle state estimation with a fusion of a low-cost imu, the gnss, radar, a camera and lidar," in *2020 IEEE/RSJ International Conference on Intelligent Robots and Systems (IROS)*. IEEE, 2020, pp. 1661–1668.
- [19] I. Belhajem, Y. B. Maissa, and A. Tamtaoui, "Improving low cost sensor based vehicle positioning with machine learning," *Control Engineering Practice*, vol. 74, pp. 168–176, 2018.
- [20] C. Chen, C. X. Lu, J. Wahlström, A. Markham, and N. Trigoni, "Deep neural network based inertial odometry using low-cost inertial measurement units," *IEEE Transactions on Mobile Computing*, vol. 20, no. 4, pp. 1351–1364, 2019.
- [21] H. Wang, C. Wang, C.-L. Chen, and L. Xie, "F-loam: Fast lidar odometry and mapping," in *2021 IEEE/RSJ International Conference on Intelligent Robots and Systems (IROS)*. IEEE, 2021, pp. 4390–4396.
- [22] Y. Cai, W. Xu, and F. Zhang, "ikd-tree: An incremental kd tree for robotic applications," *arXiv preprint arXiv:2102.10808*, 2021.
- [23] S. Zhao, H. Zhang, P. Wang, L. Nogueira, and S. Scherer, "Super odometry: Imu-centric lidar-visual-inertial estimator for challenging environments," in *2021 IEEE/RSJ International Conference on Intelligent Robots and Systems (IROS)*. IEEE, 2021, pp. 8729–8736.
- [24] C. Hertzberg, R. Wagner, U. Frese, and L. Schröder, "Integrating generic sensor fusion algorithms with sound state representations through encapsulation of manifolds," *Information Fusion*, vol. 14, no. 1, pp. 57–77, 2013.
- [25] A. L. Gibbs and F. E. Su, "On choosing and bounding probability metrics," *International statistical review*, vol. 70, no. 3, pp. 419–435, 2002.
- [26] D. He, W. Xu, and F. Zhang, "Kalman filters on differentiable manifolds," *arXiv preprint arXiv:2102.03804*, 2021.
- [27] M. Ramezani, Y. Wang, M. Camurri, D. Wisth, M. Mattamala, and M. Fallon, "The newer college dataset: Handheld lidar, inertial and vision with ground truth," in *2020 IEEE/RSJ International Conference on Intelligent Robots and Systems (IROS)*, 2020, pp. 4353–4360.
- [28] Anonymous, "Mcd viral: Visual-inertial-range-lidar multi-campus dataset with continuous-time ground truth," 11 2023. [Online]. Available: <https://mcdviral.github.io/>
- [29] A. Geiger, P. Lenz, and R. Urtasun, "Are we ready for autonomous driving? the kitti vision benchmark suite," in *2012 IEEE conference on computer vision and pattern recognition*. IEEE, 2012, pp. 3354–3361.
- [30] K. Chen, B. T. Lopez, A.-a. Agha-mohammadi, and A. Mehta, "Direct lidar odometry: Fast localization with dense point clouds," *IEEE Robotics and Automation Letters*, vol. 7, no. 2, pp. 2000–2007, 2022.